Experimental measurements of streamwise and lateral forces acting on bio-inspired pitching panels

Justin T. King ●* and Melissa A. Green ●

*Department of Aerospace Engineering and Mechanics, University of Minnesota,
Minneapolis, Minnesota 55455, USA*

The influence of planform and Strouhal number (St) on the propulsive performance of bio-inspired pitching panels is investigated for $0.09 \leqslant \text{St} \leqslant 0.66$. Aspect ratio (AR) is varied in the range $3.0 \leqslant \text{AR} \leqslant 6.6$ by changing the trailing edge sweep of a trapezoidal planform, resulting in panels of forked, straight, and pointed trailing edges. Positive mean thrust only develops for panels of reduced AR with straight or pointed trailing edges, contrary to expectations from biology. Planform and St have significant impacts on force amplitudes and improved performance is associated with larger force amplitudes. All panels experience positive thrust during significant portions of a cycle, but positive mean thrust only occurs when thrust maxima exceed drag maxima. Strong lateral forces develop for panels with the best mean performance, showing that low AR pointed panels may provide better maneuverability, as well as high thrust and efficiency. Decomposition of the thrust force into its normal and axial forces components in the frame of the panel reveal the relative impact of these components on mean performance. When mean axial forces are small or negative, a thrust-producing panel has relatively large propulsive efficiency and thrust is due primarily to normal forces. Once a thrust-producing panel reaches a local maximum in efficiency, further increases in St result in increases in mean thrust due to larger axial forces. Additionally, thrust-producing panels experience time-varying axial forces that contribute more effectively to thrust in a way not observed in forked planforms.

I. INTRODUCTION

The sphere of animal swimming is broad, ranging from microscopic creatures to the blue whale, and some animals display high swimming performance as indicated by their fast movements, large thrust, and efficient swimming [1]. Animal swimming modes exist on a spectrum from purely undulatory to purely oscillatory modes. For an oscillatory swimmer, a propulsive wave travels along the body while a caudal fin or fluke oscillates with significant amplitude at the rear of the animal [2]. The experiments in the present work are intended to represent simplifications of an oscillatory swimmer such as a thunniform swimmer, where thrust-generating movements are confined to the rear 10% of its body [3]. An understanding of the unsteady propulsion of swimming animals may prove useful for the design of novel, bio-inspired vehicles. Recently, engineers working on swimming and flying vehicles have looked to nature and have incorporated features of animal locomotion into their designs [4–12]. Bio-inspired vehicles may prove valuable in many applications, especially those typical of autonomous underwater vehicles [13,14]. Biomimicry in underwater vehicles is partially guided by a desire to outperform propeller-driven vehicles. For an MAU series propeller,

*king1526@umn.edu

053101-1

open water propulsive efficiencies tend to be $\approx 60\%$ [15], while oscillating propulsors can have efficiencies as large as 70% [16]. Propeller propulsion can also have poor maneuverability and vehicles may require multiple body lengths to execute a $180°$ turn [8]. Some swimming animals, however, can maneuver very effectively and are capable of large accelerations during turning and starting, and recent experiments have demonstrated that oscillating propulsors can create significant lateral forces that could be exploited for maneuvering [17,18].

The propulsion of a swimming animal or underwater vehicle is due to unsteady hydrodynamic forces. In particular, added mass and circulatory forces are critical for oscillatory propulsion [2], and the thrust of a purely pitching propulsor is due primarily to added mass effects from fluid accelerations around the propulsor [19]. One parameter governing propulsive performance is the Strouhal number [2], St, which can act as a nondimensional frequency representing the ratio of oscillation frequency to the flow speed [20]. Discussions in terms of St can contain information about the lateral speed of the propulsor, which has been called potentially the most important velocity scale and is not included in Reynolds number, Re, or reduced frequency, k [2]. In further support of St being a dominant parameter, the results of Triantafyllou *et al.* agree with measurements of various swimming animals that swam within $0.2 \leqslant \text{St} \leqslant 0.4$ [21]. These animals swam within this St range across a wide range of Re, providing further evidence of the role of St in performance. Similar observations were reported by Taylor *et al.*, who found that flying and swimming animals tend to cruise within $0.2 < \text{St} < 0.4$ [22]. Results from prior experiments and biology are used to select the St range of the current work, which was chosen to be $0.09 \leqslant \text{St} \leqslant 0.66$. The mean thrust of a propulsor is given by the coefficient of thrust, $C_{\overline{T}}$. In general, $C_{\overline{T}}$ is a monotonic function of St [2,17,23–26] and it scales with St^2 [2,19,27]. Changes to amplitude may lead to significant variations in $C_{\overline{T}}$, even at matching St [17,23]. For a pitching airfoil, Mackowski and Williamson measured $C_{\overline{T}}$ reductions at fixed St with increasing amplitude, and the largest amplitudes failed to generate positive thrust [17]. These results were similar to those of a rectangular flat plate, where lower pitch amplitudes resulted in greater $C_{\overline{T}}$ at similar St [23]. For rigid propulsors, mean power input ($C_{\overline{P}}$) is also a monotonic function of St; but it tends to scale with St^3 [2,27]. Das *et al.* showed that $C_{\overline{P}}$ of a pitching airfoil is relatively independent of Re, and its scaling with St^3 is primarily an inertial scaling [27].

Propulsive efficiency (η) can be calculated as the ratio of $C_{\overline{T}}$ to $C_{\overline{P}}$, and displays different behavior with respect to St than $C_{\overline{T}}$ and $C_{\overline{P}}$. Efficiency increases to a maximum at intermediate St, and then decreases inversely proportional to St [27]. Typically, the efficiency of an oscillating propulsor reaches a maximum within the St range of swimming animals [17,21], although it may lie outside this range. For example, rectangular panels reached peak η at St below the observed St range of animal swimming [23]. Simulations by Dong *et al.* on ellipsoidal foils observed peak η values at $\text{St} \geqslant 0.4$, and this relatively large St for peak η was attributed to the low Re [28]. Performance can also be influenced by factors like kinematics, shape, and material properties. Efficiencies of rigid purely pitching propulsors in isolation are usually low, typically not exceeding 20%. For example, a pitching airfoil achieved peak η of 12% [17], a flat plate produced maximum η of 13% [29], and a NACA-0012 airfoil reached a peak η of 16% [27]. Efficiency can be improved through kinematic changes like the introduction of heave with a phase delay. For a phase delay of $270°$, Van Buren *et al.* measured increases in $C_{\overline{T}}$ and η as large as approximately 40% [30]. Large efficiencies have also been measured by Read *et al.*, who observed an η of 71.5% when the phase lag between heave and pitch was optimized [16].

Changes to planform and aspect ratio (AR) can impact performance, and reductions in AR often cause performance degradation [2]. Simulations have found that reductions in AR for ellipsoidal foils decrease peak η, with a foil of infinite AR having a peak η approximately 50% larger than a low AR foil [28]. However, increases in AR created diminishing returns in performance gains, with improvements most noticeable at low AR. Similarly, rectangular pitching panels of $0.54 \leqslant \text{AR} \leqslant 2.38$ displayed a monotonic relationship between $C_{\overline{T}}$ and AR [23]. Changes to planform shape can also impact performance as shown by experiments on constant AR pitching panels by Van Buren *et al.* [31] that were later validated numerically by Hemmati *et al.* [32]. Trailing edge variations were

introduced to a rectangular planform, and it was found that a pointed trailing edge produced the best performance. These findings are contrary to expectations from biology that anticipate superior performance for forked planforms. Similar findings were observed by Zhang *et al.*, who found η increased as the trailing edge became more pointed for self-propelled flexible panels in pure heave [33]. The effects of trailing edge shape on performance were also measured by Feilich and Lauder, who found that a foil with large peduncle and vertical trailing edge had the highest self-propelled swimming speed [34]. At least four distinct lineages of high performance swimming animals have propulsors of high AR and forked or lunate planform [1,35,36]. The independent development of similar planforms supports the notion that those shapes represent an evolutionary culmination in swimming performance [1,35–37], and it would be reasonable to speculate that an optimal propulsor should be of high AR and lunate or forked in shape. The contrast of these evolutionary observations to the laboratory or simulation results of Van Buren *et al.*, Hemmati *et al.*, and Zhang *et al.*, therefore, warrants further investigation.

The current work investigates whether the performance results of Van Buren *et al.* [31] extend to planforms with swept leading edge (trapezoidal) and varying trailing edge shape. Furthermore, we present quasi-time-resolved forces for different planforms, and the decomposition of these forces into normal and axial components. In particular, we are interested in the magnitude and timing of these components and their contributions to thrust and lateral forces. Mean performance results, e.g., $C_{\overline{T}}$ and η, are frequently reported in the experimental literature, but time-varying forces are more rare, with Mackowski and Williamson claiming in 2015 to be unaware of prior experimental treatment [17]. This statement is not entirely correct, as time-resolved forces on a heaving flexible panel were reported by Quinn *et al.* [38]. Subsequently, other time-varying force results from experiments and simulations have appeared in the literature [26,32,39,40]. For periodic motions, lateral forces tend to vary with the motion frequency, while the streamwise forces vary at twice the motion frequency. For pure pitch, thrust maxima occur soon after the propulsor reaches a pitching extreme, and thrust minima occur shortly after the propulsor crosses the wake centerline. These trends appear to be quite consistent, even when material and planform shape are changed. The experiments of the current work seek to elucidate characteristics of time-varying and time-averaged forces that act on purely pitching panels with bio-inspired planforms.

II. EXPERIMENTAL SETUP AND METHODOLOGY

Experiments used five panels of 1/16 in. thick acrylic whose planforms mimic cetacean flukes and caudal fins like those in Fig. 1(a). All panels are classified as either forked, straight, or pointed according to trailing edge shape. Each planform is based on a trapezoid, but with changes to trailing edge sweep for all but one panel. Figure 1(b) displays a schematic of the variables used to define the planform shape. Leading edge sweep angle is given by θ_1, trailing edge sweep angle by θ_2, front edge length by a, tip-to-tip span by b, and midspan chord length by c. θ_1 was fixed at $45°$ while θ_2 was varied from $-20°$ to $20°$ in increments of $10°$. The front edge, a, had a length of 52 mm and the trailing edge, b, was 254 mm. The AR of a panel is defined by $\text{AR} = b^2/S$, where S is the planform area. The AR range, $3.0 \leqslant \text{AR} \leqslant 6.7$, was selected to overlap with caudal fin characteristics of various fish species [41,42]. Reynolds number is based on midspan chord according to $\text{Re}_c = Uc/\nu$, where ν is kinematic viscosity, and the free stream speed was $U = 160$ mm/s for all experiments. A summary of geometric parameters and Re_c is given by Table I, which also introduces the panel numbering convention. Panels 1 and 2 are forked geometries with a concave trailing edge. Panel 3 has a straight trailing edge and is identical to a trapezoid, while panels 4 and 5 are pointed panels with a convex trailing edge. The numbering scheme corresponds to trailing edge convexity, i.e., the trailing edge becomes more pointed with increasing panel number. For additional reference to planform details, to-scale illustrations of all panels are found in Fig. 1(c).

Panels were sinusoidally pitched about their leading edge in a uniform free stream according to $\phi(t) = \phi_{\max} \sin(2\pi f t)$, where $\phi_{\max}$ is the angular amplitude. Instantaneous pitch angle, ϕ, is defined so that when $\phi = 0°$ the panel is parallel to the free stream. Accordingly, the panel is in the
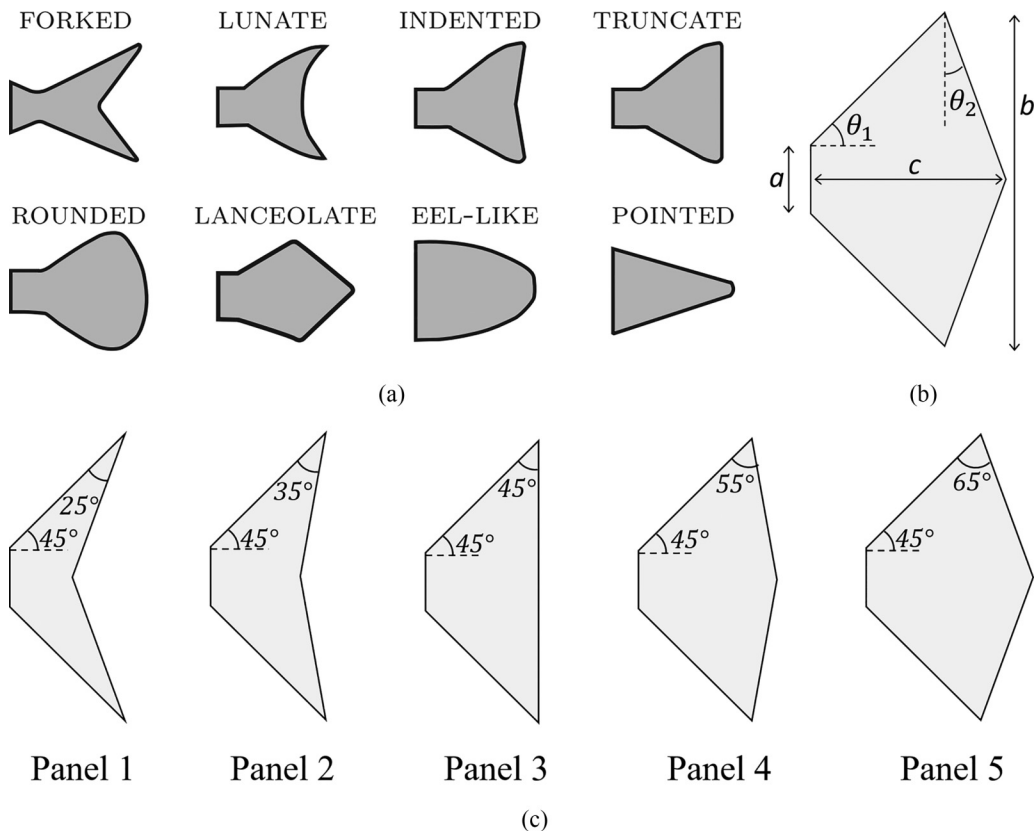
FIG. 1. (a) Planform abstractions of caudal fins and cetacean flukes. Adapted from Van Buren *et al.* [31]. (b) Variables used to characterize planform. Leading edge sweep is θ_1, trailing edge sweep is θ_2, front edge length is a, tip-to-tip span is b, and midspan chord length is c. (c) To-scale schematics of all planforms. Leading edge sweep angle is $45°$ while trailing edge sweep varies.

$+y$ domain when $\phi > 0°$ and in the $-y$ domain when $\phi < 0°$. As described in Table II, five values of ϕ_{max}, ranging from 5–25° in increments of 5° were used. The pitching frequency, f, had a constant value of 1 Hz and Strouhal number is calculated as $\mathrm{St} = f\overline{A}/U$, where $\overline{A}$ is the average trailing edge amplitude across the span. By using $\overline{A}$ to define St, differences in average trailing edge speeds among panels is captured even when ϕ_{max} is equal. For a given panel, St is altered through changes to ϕ_{max}, since f and U are constant. The St range, $0.09 \leqslant \mathrm{St} \leqslant 0.66$, was selected to overlap with observations of animal swimming, which correspond to $0.2 \leqslant \mathrm{St} \leqslant 0.4$ [21,22].

TABLE I. Geometric parameters and Re_c used during experiments.

Panel no.	Description	$\theta_1(°)$	$\theta_2(°)$	c (mm)	AR	$\mathrm{Re}_c(\times 10^3)$
1	Forked	45	−20	54.8	6.7	8.8
2	Forked	45	−10	78.6	5.1	12.6
3	Straight	45	0	101	4.2	16.2
4	Pointed	45	10	123.4	3.5	19.7
5	Pointed	45	20	147.2	3.0	23.6

TABLE II. Review of $\phi_{\max}$ and their associated St for all five panel geometries during experiments.

$\phi_{\max}$ (°)	St				
	Panel 1	Panel 2	Panel 3	Panel 4	Panel 5
5	0.09	0.10	0.11	0.12	0.14
10	0.17	0.20	0.22	0.24	0.27
15	0.25	0.29	0.33	0.36	0.40
20	0.33	0.38	0.43	0.48	0.53
25	0.41	0.47	0.53	0.59	0.66

All experiments were conducted in a recirculating water tunnel with a cross section of 0.61 m by 0.61 m and a length of 2.44 m. A schematic of the water tunnel test section during performance measurements is shown in Fig. 2. Upstream of the test section, flow was conditioned by a honeycomb flow straightener and four mesh screens. The pitching shaft was made of stainless steel and designed to minimize shaft deflections from panel forces by using a stepped shaft with relatively large base diameter. A not-to-scale schematic of the pitching shaft is shown in Fig. 3. A tab on the leading edge of each panel was inserted into the 0.25 in. diameter pitching shaft, which sat inside of a 0.5 in. diameter shaft. The larger shaft was far enough away from the panel to eliminate the presence of vortices caused by the diameter change [43]. The 0.5 in. diameter shaft was attached to the measurement surface of the force-torque transducer, while the opposite transducer surface connected the entire assembly to the motor output shaft. The pitching motor was controlled by a Galil DMC-4123 motion controller and an encoder with resolution of 1024 counts per revolution.

Time-resolved force and torque measurements were collected with a Mini40 transducer manufactured by ATI Industrial Automation with an IP68 rating. Prior to data collection, the transducer calibration was validated through static and dynamic tests in air. For the static tests, known masses were used to compare transducer measurements to expected gravitational forces. For the dynamic tests, an aluminum plate of known mass and geometry was actuated through sinusoidal motions using methodology adapted from DeVoria [44]. For each St in Table II, 20 individual runs of performance data were collected at 1000 Hz for 36 pitching cycles. To minimize transient effects, data from the first five cycles and the last cycle were disregarded.

The procedure for an individual run is summarized as follows. With the water stationary, the panel was moved to $\phi = 0°$ and the transducer readings were tared, and the flow speed was brought to to its appropriate value and drag on the stationary panel and shaft was measured. Then, 36 pitching cycles for each $\phi_{\max}$ were completed, and the process was repeated for 20 total runs. Inertial forces and torques were also measured in air and found to be relatively small, with peak hydrodynamic forces as much as 40 times greater than the largest inertial forces. All measurements were filtered using *filtfilt* in MATLAB for a second order, lowpass Butterworth filter with a lowpass
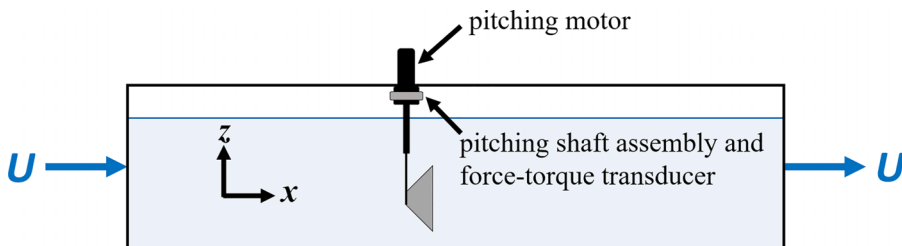

FIG. 2. Schematic of water tunnel during performance measurement experiments. A pitching motor above the tunnel free surface was used to actuate a pitching shaft attached to the leading edge of a panel.
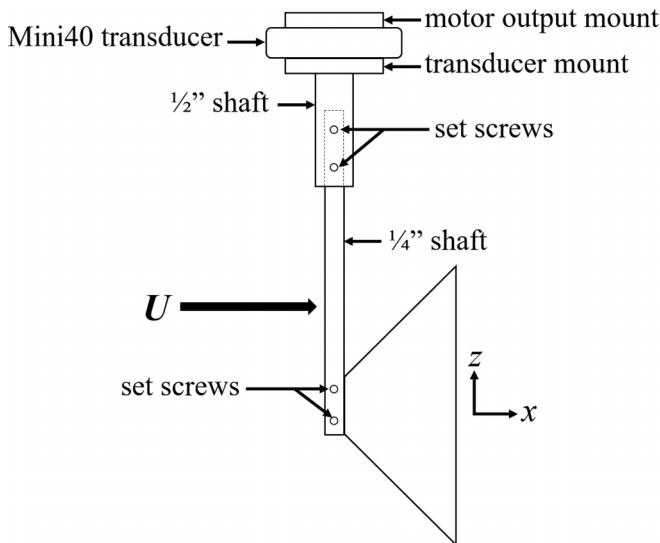
FIG. 3. Not-to-scale schematic of the pitching shaft assembly. The shaft is similar to a stepped cylinder and was designed to minimize unwanted shaft deflections. Flow is from left to right.

cutoff frequency of 50 Hz. All 20 individual runs for air and water were phase-averaged and final data then obtained by subtracting air measurements and shaft drag from the water tunnel results.

III. RESULTS

A. Time-averaged propulsive performance

Mean thrust and propulsive efficiency are used to establish relationships between performance, planform, and kinematics. Mean thrust is given by the nondimensional coefficient of thrust, $C_{\overline{T}} = 2\overline{T}/(\rho U^2 S)$, where $\overline{T}$ is mean dimensional thrust over a cycle and ρ is the fluid density. Propulsive efficiency is given by a Froude efficiency, $\eta = C_{\overline{T}}/C_{\overline{P}}$, where the nondimensional coefficient of power is $C_{\overline{P}} = 2\overline{T}/(\rho U^3 S)$. $C_{\overline{T}}$ and η as functions of St are shown in Fig. 4, where errors bars are the standard error of the mean. As St increases, panels 3–5 experience a monotonic rise in $C_{\overline{T}}$, while forked panels fail to create positive $C_{\overline{T}}$ and tend to lose thrust with St. In similar works, $C_{\overline{T}}$ has also been found to increase monotonically with St [2,17,23–26]. Thrust can also vary nonlinearly with St, scaling instead with St^2 [2,19,27]. In Fig. 4(a), $C_{\overline{T}}$ varies with St^2 for panels 3–5, which becomes more recognizable as panel number increases. The reduction in $C_{\overline{T}}$ for forked panels with St may be due in part to an increase in quasisteady drag on the panel. Prior experimental work has shown that larger pitch amplitudes can produce greater quasisteady viscous drag [30]. Accordingly, for the forked panels in the current work, viscous drag may increase with pitching amplitude and St more rapidly than thrust, causing $C_{\overline{T}}$ to decrease with St. $C_{\overline{T}}$ may increase despite AR reductions, demonstrating that planform changes that reduce AR do not necessarily lead to performance degradation. The results for $C_{\overline{T}}$ in Fig. 4(a) are consistent with prior works on varying trailing edge shape that reported increased performance in association with increased trailing edge convexity [31,32]. The $C_{\overline{T}}$ trends of the forked panels in the current work, however, differ from those of Van Buren *et al.*, which generated positive mean thrust [31].

For thrust-producing panels, η achieves a local maximum at intermediate St in the range $0.22 \leqslant St \leqslant 0.27$, which lies towards the lower end of the observed range for animal swimming [21,22]. At St above this range, increases in St result in reductions in η. For thrust-producing panels, the largest observed η occurs at an intermediate amplitude of $\phi_{max} = 10°$. Overall, η values tend to be relatively low, attaining a maximum value of 14.4%. Peak η values for a thrust-producing panel
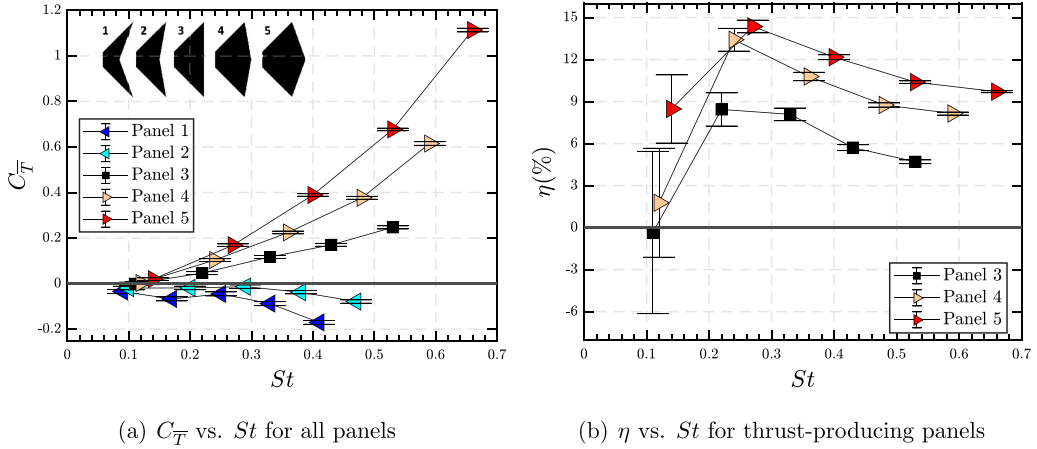
(a) $C_{\overline{T}}$ vs. St for all panels

(b) η vs. St for thrust-producing panels

FIG. 4. Variation in $C_{\overline{T}}$ for all panels and η for only thrust-producing panels at their respective St Panel 1, $0.09 \leqslant St \leqslant 0.41$; Panel 2, $0.10 \leqslant St \leqslant 0.47$; Panel 3, $0.11 \leqslant St \leqslant 0.53$; Panel 4, $0.12 \leqslant St \leqslant 0.59$; Panel 5, $0.14 \leqslant St \leqslant 0.66$. $C_{\overline{T}}$ and to-scale schematics of panel planforms are shown in (a), and η values are shown in (b).

decrease as AR increases, again illustrating that performance can be improved through planform changes despite AR reductions. The efficiency results in Fig. 4(b) for panels 3–5 agree with prior work linking increased trailing edge convexity to with increased efficiency [31,32]. Overall, mean performance results disagree with expectations from animal swimming, where high AR forked propulsors are linked with high performance. Engineers seeking to incorporate bio-inspired propulsors into oscillatory propulsion should use caution when using direct mimicry of nature as there may be scenarios where low AR, pointed propulsors could prove beneficial.

The performance data shown in Fig. 4 are nondimensionalized using the dynamic pressure of the free stream. Although the nondimensionalizations used in $C_{\overline{T}}$ and $C_{\overline{P}}$ contain information about planform area, they do not capture parameters like leading and trailing edge sweep. Trailing edge sweep, as well as planform area, can be captured by using a nondimensionalization of mean thrust that takes into account the lateral velocity of the trailing edge. Accordingly, a new coefficient of thrust, $C_{\overline{T}}^{*}$, can be defined according to $C_{\overline{T}}^{*} = \overline{T}/[\rho(f\overline{A})^2 S]$. Note that for the panels in the current work, $(f\overline{A})^2$ tends to increase as the trailing edge becomes more pointed and the mean trailing edge velocity increases due to increased chord length and movement of the geometric center of the panel away from the pitching axis. This same nondimensionalization was also applied by Van Buren $et\ al.$ to performance data on two-dimensional pitching and heaving rectangular foils [45]. Results for $C_{\overline{T}}^{*}$ as a function of St for all panels are shown in Fig. 5, which reveals that $C_{\overline{T}}^{*}$ becomes approximately constant with St once $\overline{A}$ and lateral trailing edge velocity become large enough, indicating that changes in trailing edge velocity result in proportional changes to mean dimensional thrust. This behavior in $C_{\overline{T}}^{*}$ always occurs regardless of whether a panel produces positive mean thrust or not. The use of $C_{\overline{T}}^{*}$ in Fig. 5 supports the findings of Van Buren $et\ al.$ [45], who found that the mean velocity of the trailing edge provides a better scaling for propulsive performance than the free stream velocity. The results of the current work bolster these previous findings on two-dimensional foils by demonstrating that $C_{\overline{T}}^{*}$ is an appropriate thrust scaling for three-dimensional, bio-inspired propulsors provided that the mean trailing edge velocity is large enough.

Although Fig. 5 indicates that mean thrust data plateau at a constant value across St for a given planform when a trailing edge velocity scaling is used, there is still significant variation in $C_{\overline{T}}^{*}$ among panel geometries. Additional work is needed to better understand what role planform shape plays in thrust develop, which may lead to new scalings that better collapse the data for $C_{\overline{T}}^{*}$. For the
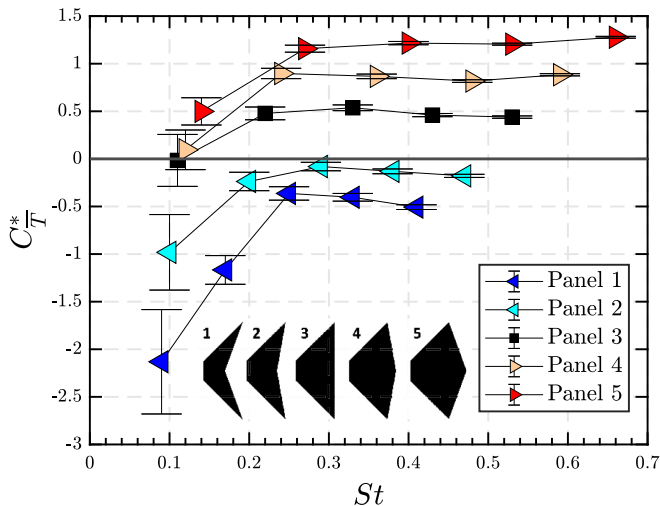
FIG. 5. Variation in $C_{\overline{T}}^*$ for all panels at their respective St: panel 1, $0.09 \leqslant St \leqslant 0.41$; panel 2, $0.10 \leqslant St \leqslant 0.47$; panel 3, $0.11 \leqslant St \leqslant 0.53$; panel 4, $0.12 \leqslant St \leqslant 0.59$; panel 5, $0.14 \leqslant St \leqslant 0.66$. To-scale schematics of panel planforms shown at bottom of figure.

three-dimensional planforms of the current work, geometric and kinematic parameters, besides just planform area and trailing edge velocity, play a role in propulsive performance. The scalings used for mean performance data in Figs. 4 and 5 do take into account planform area, but they fail to capture factors such as: leading edge sweep angle, leading and trailing edge curvature, swept area, AR, cross-section, etc. For the panels of the current work, many of these parameters, e.g., AR and trailing edge sweep angle, are changed simultaneously, and it is difficult isolate their influence on propulsive performance. To account for the impact of variables like these, three-dimensional scaling laws are necessary. Recently, there have been three-dimensional approaches [46,47] that expand upon earlier two-dimensional approaches at performance scaling [19,48–50]. These three-dimensional approaches reveal that the added mass of the propulsor, upwash, and downwash of the wake, and topology of wake vortices all impact performance. Furthermore, there is evidence that optimal propulsor shape and kinematics are interdependent, and may be tailored to each other in the case of swimming mammals [47]. Ultimately, it is difficult to decouple the individual influences of AR and planform shape in the current work, but continued work three-dimensional scaling laws that apply to a broad range of propulsor shapes may help elucidate these details.

B. Time-varying thrust and lateral forces

Time-varying forces can be important for maneuverability and agility, and may impact mean thrust and efficiency. Despite their impact on swimming, time-varying forces are not frequently reported in the experimental research literature. The time-varying coefficient of thrust is given by $C_{\widehat{T}} = 2\widehat{T}/\rho U^2 S$, where instantaneous thrust is $\widehat{T}$. In this work, the values of $\widehat{T}$ are given in terms of phase-averaged thrust, which is treated as representative of instantaneous thrust. For select panels at their respective St, $C_{\widehat{T}}$ measurements as a function of time during a pitching cycle are shown in Fig. 6. In Fig. 6 and some subsequent figures, the time during the pitching cycle is given by t/T, where t is the dimensional time and T is the pitching period. According to the sinusoidal motion profile introduced in Sec. II, $t/T = 0$ and $t/T = 0.5$ correspond to $\phi = 0°$, while $t/T = 0.25$ and $t/T = 0.75$ correspond to $\phi = +\phi_{max}$ and $\phi = -\phi_{max}$, respectively. $C_{\widehat{T}}$ varies at twice the pitching frequency and peak thrust occurs as the panel retreats from a motion extreme when $t/T \approx 0.35$ and $t/T \approx 0.85$. Positive $C_{\widehat{T}}$ develops near a motion extreme and it remains positive
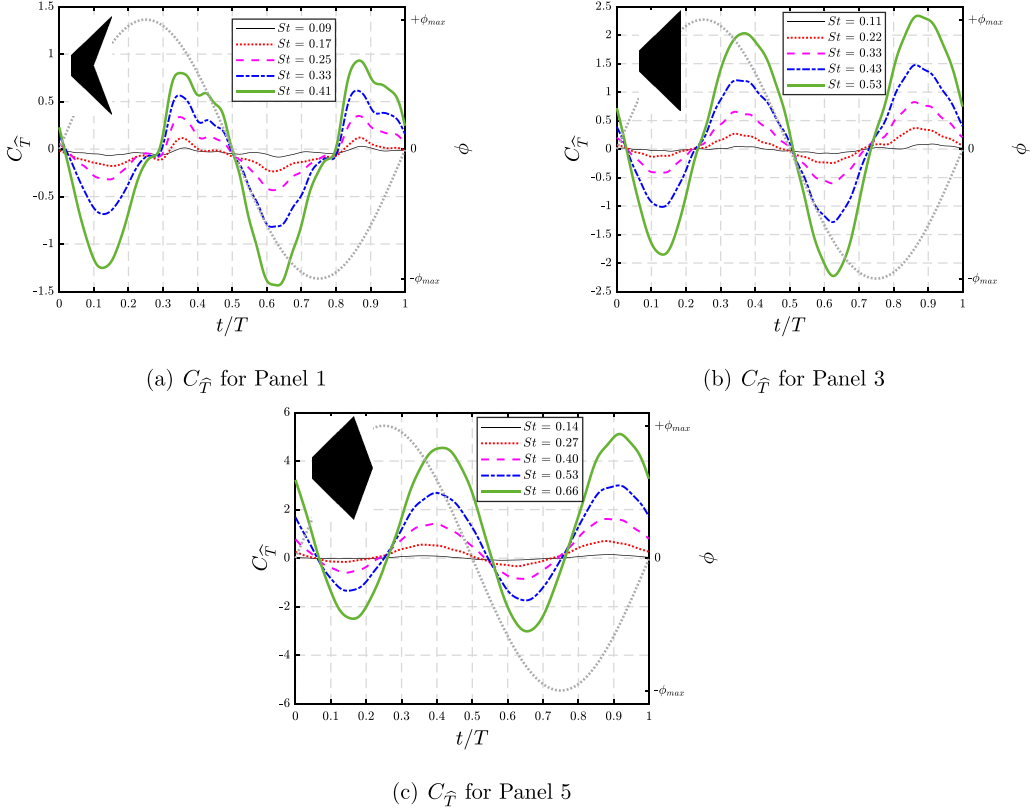
(a) $C_{\widehat{T}}$ for Panel 1

(b) $C_{\widehat{T}}$ for Panel 3

(c) $C_{\widehat{T}}$ for Panel 5

FIG. 6. Variation in $C_{\widehat{T}}$ during a cycle for panel 1, panel 3, and panel 5 at their respective St: (a) panel 1, $0.09 \leqslant \mathrm{St} \leqslant 0.41$; (b) panel 3, $0.11 \leqslant \mathrm{St} \leqslant 0.53$; (c) panel 5, $0.14 \leqslant \mathrm{St} \leqslant 0.66$. The angular position of the panel is shown in gray. To-scale schematics of panel planforms shown in each subfigure.

until the panel crosses the wake centerline. $C_{\widehat{T}}$ minima occur shortly after the panel crosses the wake centerline when $t/T \approx 0.15$ and $t/T \approx 0.65$. Similar timings have been reported for experiments on pitching propulsors of different planforms [32,39], showing that geometry changes appear to have little influence on thrust timings. The phase of $C_{\widehat{T}}$ with respect to the panel motion shows slight sensitivity to geometry and St, and $C_{\widehat{T}}$ generally lags panel motion within the approximate range of $30°$ to $60°$. However, thrust-producing panels experience their smallest phase lags when η is relatively large, but further increases in St (and therefore decreases in η) are associated with greater phase lags. Given the similarities in $C_{\widehat{T}}$ timings among geometries, the influence of planform and St on mean performance should not be attributed to changes in the phase of $C_{\widehat{T}}$ with respect to the panel motion.

$C_{\widehat{T}}$ maxima of a panel increase with St and more pointed panels tend to produce larger $C_{\widehat{T}}$ peaks, even at similar St. Comparison of $C_{\widehat{T}}$ traces among panels in Fig. 6, for example between panels 1 and 3 at St $= 0.33$, reveals that forked panels rapidly lose thrust as higher frequency oscillations in $C_{\widehat{T}}$ develop. Figure 6(a) further demonstrates that these secondary oscillations develop for panel 1 at all St. These secondary $C_{\widehat{T}}$ oscillations are not significant for thrust-producing panels, however, and they likely benefit from their absence. For panel 1, shortly after $t/T \approx 0.3$ and $t/T \approx 0.8$, the secondary $C_{\widehat{T}}$ oscillations arise and $C_{\widehat{T}}$ declines quickly so that instances of $C_{\widehat{T}}$ maxima correspond to the onset of secondary $C_{\widehat{T}}$ oscillations. This causes the peak phase-averaged thrust to appear earlier in the cycle, and with a lower maximum value than it otherwise might have.

As will be discussed in Sec. III C, secondary $C_{\widehat{T}}$ oscillations are ultimately due to high frequency oscillations in chordwise axial forces acting on the forked panels. Near motion extremes, increasing $C_{\widehat{T}}$ for forked panels is interrupted by a temporary decrease in thrust, which becomes more pronounced at larger St. A similar phenomenon was observed by Hemmati *et al.*, who attributed this thrust irregularity to momentum transfer associated with the direction change of the panel [32]. More pointed panels are better able to increase $C_{\widehat{T}}$ throughout direction changes, further benefiting the propulsive performance of nonforked planforms.

All scenarios are plagued by significant drag for approximately half a pitching cycle, which is typical of rigid panels. For forked panels, drag maxima exceed $C_{\widehat{T}}$ maxima and their difference grows with St, but panels 3–5 have $C_{\widehat{T}}$ maxima that always exceed drag maxima, consistent with their production of positive mean thrust. $C_{\widehat{T}}$ always oscillates with double the pitching frequency, regardless of the sign or magnitude of mean thrust, and $C_{\widehat{T}}$ amplitude scales nonlinearly with St, in agreement with previously reported observations of $C_{\overline{T}}$ [2,19,27]. Increases in $C_{\widehat{T}}$ amplitude alone are not sufficient to produce positive mean thrust, as $C_{\widehat{T}}$ amplitudes of forked panels can be similar to those of panels 3–5 at similar St, yet forked panels experience negative $C_{\overline{T}}$. For example, when panel 1 pitches at St = 0.33, the $C_{\widehat{T}}$ traces in Fig. 6(a) have an approximate amplitude of 0.75, which is similar to the $C_{\widehat{T}}$ amplitude of panel 3 at the same St. Similar results occur at higher St, where panel 1 at St = 0.41 and panel 5 at St = 0.40 both experience $C_{\widehat{T}}$ amplitudes of approximately 1.25, despite their diverging time-averaged thrust behaviors. Forked panels of high AR are able to generate fluctuating thrust forces as effectively as the other planforms; however, $C_{\widehat{T}}$ fluctuates around a negative mean. Subsequent discussion will illustrate how the mean thrust of forked planforms is degraded by normal forces on the panel that inhibit positive thrust production. Reductions in $C_{\overline{T}}$ cannot be attributed solely to increased viscous drag, as measurements show static drag increases with panel number. It is worth noting that all experiments were done at the same free stream speed, and therefore Re effects on the mean thrust-drag balance should not be an issue.

Mean lateral forces are typically of little interest as they are zero for a symmetric motion, except when deflected wakes occur [51,52]. However, instantaneous lateral forces may introduce recoil reactions in swimming fish and can be useful for maneuverability [53]. Time-varying lateral force is denoted by $C_{\widehat{L}} = 2\widehat{L}/\rho U^2 S$, where instantaneous lateral force is $\widehat{L}$. In this work, the values of $\widehat{L}$ are given in terms of phase-averaged lateral force, which is treated as representative of instantaneous lateral force. $C_{\widehat{L}}$ during a cycle for all panels and St is shown in Fig. 7. Much like $C_{\widehat{T}}$, the qualitative behavior of $C_{\widehat{L}}$ is rather insensitive to planform and St. Lateral forces oscillate with the pitching frequency and peak magnitude $C_{\widehat{L}}$ occurs when $t/T \approx 0$ and $t/T \approx 0.5$ as the panel pitches with maximum angular speed. Near-zero $C_{\widehat{L}}$ develops near motion extremes as the panel moves with approximately zero angular speed and large magnitude angular acceleration. The lateral force timings of the current work generally agree with simulations of a pitching airfoil that found peak magnitude $C_{\widehat{L}}$ when $t/T \approx 0.4$ and $t/T \approx 0.9$ [39]. For nonforked panels, peak magnitude $C_{\widehat{L}}$ tends to develop later in the cycle as St increases, but the influence of St on $C_{\widehat{L}}$ timings is not as evident for panel 1, which experiences nonnegligible higher frequency fluctuations in $C_{\widehat{L}}$. These fluctuations do not develop for other panels at low St, even though peak magnitude $C_{\widehat{L}}$ are similar. Peak $C_{\widehat{L}}$ can become considerably larger than peak $C_{\widehat{T}}$ for a given panel and St, and larger panel number and St result in larger magnitude $C_{\widehat{L}}$ peaks. Lateral forces can be used for turning and other maneuvers, but may prove undesirable for straight line locomotion. The strongest lateral forces develop for panels with the best mean performance, showing that low AR pointed panels could also provide better maneuverability with improved forward propulsion. However, there is a tradeoff between efficiency and maneuverability for thrust-producing panels. The strongest lateral forces develop at high St when propulsive efficiency is below its peak value.

C. Axial and normal panel forces

Time-varying forces can be investigated in the rotating reference frame of the panel. Thrust in the streamwise direction can be decomposed into contributions from the normal and chordwise forces
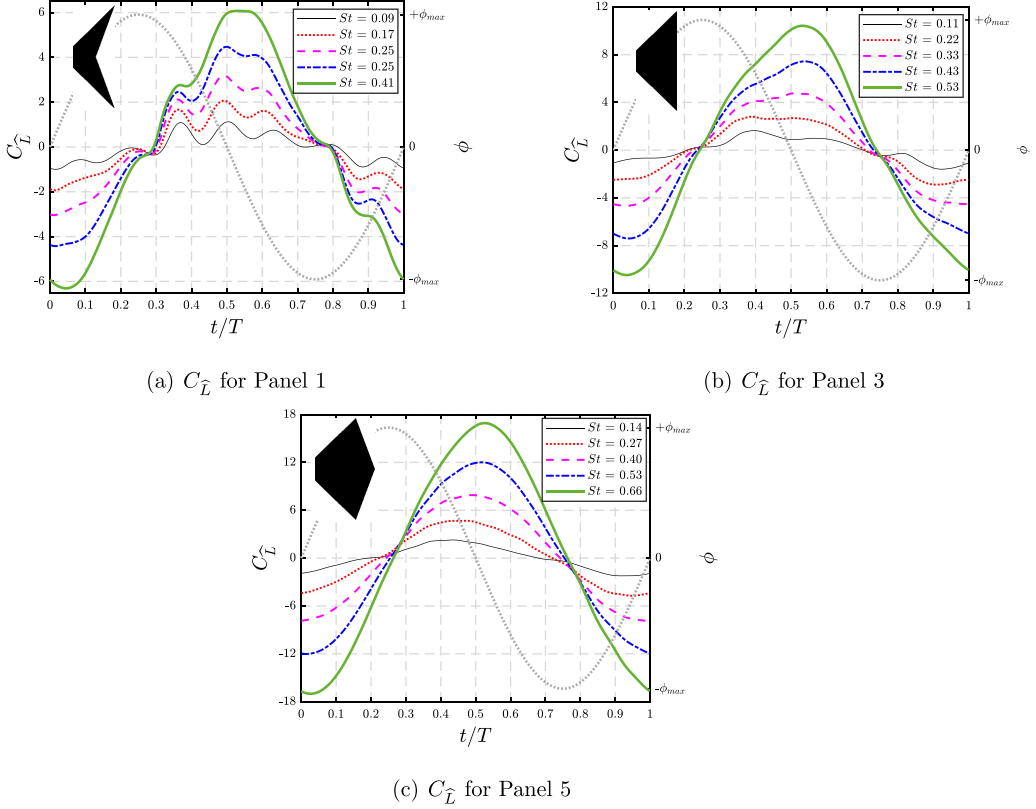
(a) $C_{\widehat{L}}$ for Panel 1

(b) $C_{\widehat{L}}$ for Panel 3

(c) $C_{\widehat{L}}$ for Panel 5

FIG. 7. Variation in $C_{\widehat{L}}$ during a cycle for panel 1, panel 3, and panel 5 at their respective St: (a) panel 1, $0.09 \leqslant \mathrm{St} \leqslant 0.41$; (b) panel 3, $0.11 \leqslant \mathrm{St} \leqslant 0.53$; (c) panel 5, $0.14 \leqslant \mathrm{St} \leqslant 0.66$. The angular position of the panel is shown in gray. To-scale schematics of panel planforms shown in each subfigure.

acting on the panel as described by David *et al.* for their experiments on rectangular foils pitching at small angles [40]. Instantaneous thrust can be viewed as the sum of these two components according to Eq. (1), where instantaneous normal force is $C_{\widehat{N}}$ and instantaneous axial force is $C_{\widehat{A}}$,

$$C_{\widehat{T}} = C_{\widehat{TA}} + C_{\widehat{TN}} = C_{\widehat{A}} \cos \phi + C_{\widehat{N}} \sin \phi. \tag{1}$$

Instantaneous thrust can then be manipulated to yield time-averaged thrust as in Eq. (2):

$$C_{\overline{T}} = C_{\overline{TA}} + C_{\overline{TN}} = \overline{C_{\widehat{A}} \cos \phi} + \overline{C_{\widehat{N}} \sin \phi}. \tag{2}$$

In Eqs. (1) and (2), chordwise axial forces on the panel are considered positive when they are directed upstream towards the leading edge and positive normal forces are orthogonal to the positive axial axis with the z axis pointed upwards. For small pitching amplitudes, normal and axial forces have also been investigated by Floryan *et al.* using scaling laws based on added mass effects [19].

The normal and axial force contributions to time-averaged thrust for all panels and St are shown in Fig. 8. The behaviors of $C_{\overline{TA}}$ and $C_{\overline{TN}}$ depart significantly from those previously reported in the research literature for pitching rectangular planforms at small amplitudes. For the rectangular planforms of David *et al.*, $C_{\overline{TN}}$ was much larger than $C_{\overline{TA}}$ at all St, and $C_{\overline{TA}}$ was always negative [40]. In the current work, axial forces can contribute greatly towards the positive mean thrust, which becomes more pronounced as pitching amplitude and St increase. When $\mathrm{St} < 0.27$, all panels experience negative $C_{\overline{TA}}$, in agreement with the small angle results of David *et al.* [40]. However, as amplitude and St increase, $C_{\overline{TA}}$ becomes positive and larger for all panels and the rise
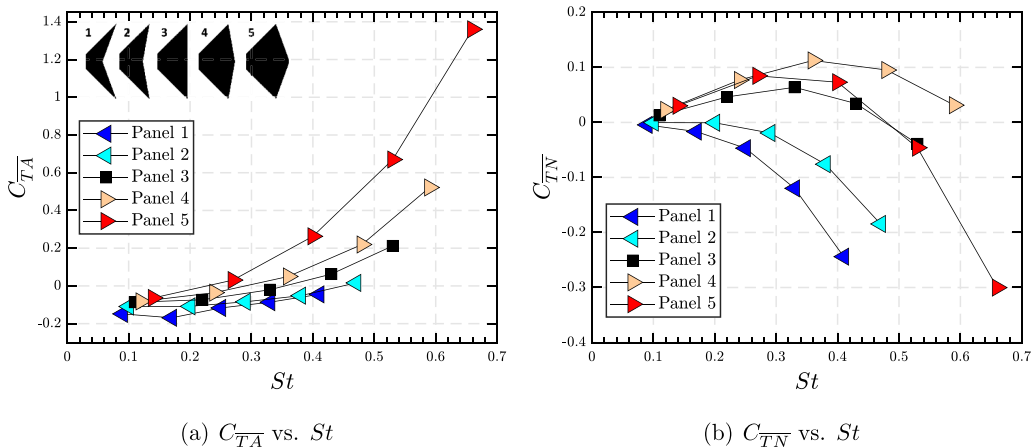
(a) $C_{\overline{TA}}$ vs. St

(b) $C_{\overline{TN}}$ vs. St

FIG. 8. Variation in $C_{\overline{TA}}$ and $C_{\overline{TN}}$ for all panels at their respective St Panel 1, $0.09 \leqslant St \leqslant 0.41$; Panel 2, $0.10 \leqslant St \leqslant 0.47$; Panel 3, $0.11 \leqslant St \leqslant 0.53$; Panel 4, $0.12 \leqslant St \leqslant 0.59$; Panel 5, $0.14 \leqslant St \leqslant 0.66$. $C_{\overline{TA}}$ and to-scale schematics of panel planforms shown in (a), and $C_{\overline{TN}}$ values are shown in (b).

in $C_{\overline{TA}}$ is accompanied by a significant increase in $C_{\overline{T}}$ for only thrust-producing panels. Shortly after propulsive efficiency tends to degrade for panels 3–5, $C_{\overline{TA}}$ rises rapidly in a nonlinear manner with further increases in St.

Contrasting behaviors develop for $C_{\overline{TN}}$, which ultimately becomes negative for all panels except panel 4 as St increases. For forked planforms, $C_{\overline{TN}}$ is always negative and becomes more negative as St increases, acting to reduce $C_{\overline{T}}$. This demonstrates that the inability of forked panels to produce positive mean thrust is due to the behaviors of normal forces. Even though mean $C_{\overline{TA}}$ does increase with St for forked panels, $C_{\overline{TA}}$ never becomes strong enough to counteract the negative influence of $C_{\overline{TN}}$. As shown in Fig. 8(a), negative $C_{\overline{TA}}$ does not strictly indicate negative mean thrust. At low St, panels 3–5 counteract below-zero axial forces through positive $C_{\overline{TN}}$, something panels 1 and 2 are unable to do. For thrust-producing geometries, Fig. 8(b) reveals that $C_{\overline{TN}}$ rises with St until reaching a peak measured value at $\phi_{\max} = 15°$ when St are slightly higher than those associated with peak efficiency. Further increases in St result in dramatic degradations in $C_{\overline{TN}}$, which are most extreme for panel 5. When St $= 0.66$, panel 5 pitches with a global minimum in $C_{\overline{TN}}$, yet this case represents the global maximum in $C_{\overline{T}}$ due to the global maximum in $C_{\overline{TA}}$. The only other thrust-producing panel to experience negative $C_{\overline{TN}}$ is panel 3 at St $= 0.53$.

At larger pitching amplitudes, panels 3–5 develop positive mean thrust either mostly or exclusively through axial forces. In certain scenarios, normal forces diminish mean thrust production for these panels as is the case for panels 3 and 5 at their highest St. The results for $C_{\overline{TA}}$ and $C_{\overline{TN}}$ indicate that the manner of mean thrust production depends on St for thrust-producing geometries and it can be divided into two regimes. At low St mean axial forces are small in magnitude, and they also tend to be negative and reduce mean thrust while $C_{\overline{TN}}$ dominates. Conditions where $C_{\overline{TA}}$ are near-zero or negative and $C_{\overline{TN}}$ is large correspond to scenarios of relatively large η for a thrust-producing panel. Once a thrust-producing panel reaches a local maximum in η, further increases in St result in a nonlinear increase in $C_{\overline{TA}}$, which is accompanied by a rapid decrease in $C_{\overline{TN}}$. These behaviors at high St are characteristic of the second regime, where positive $C_{\overline{T}}$ is due primarily to axial forces and may even be reduced by normal forces. For thrust-producing panels, the transition between regimes occurs through increases in St and is associated with greater lag between $C_{\widehat{T}}$ and the panel motion. This lag continues to grow with increases in St after a $C_{\overline{TN}}$ maximum is reached.

As with discussions of $C_{\widehat{T}}$ and $C_{\widehat{L}}$, it is useful to discuss the time-varying axial and normal force contributions and their influence on mean thrust. The time-varying, instantaneous axial and normal forces are denoted by $C_{\widehat{TA}}$ and $C_{\widehat{TN}}$, respectively. Traces of $C_{\widehat{TA}}$ for select panels at their respective St

(a) $C_{\widehat{TA}}$ for Panel 1

(b) $C_{\widehat{TA}}$ for Panel 3
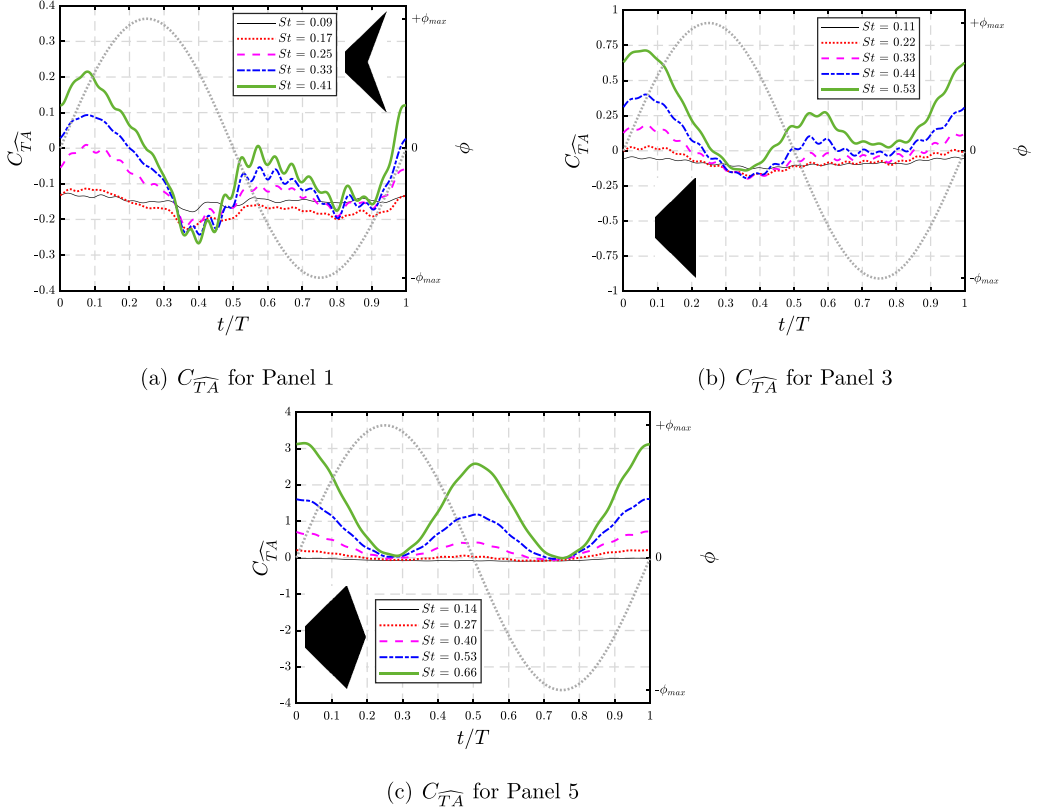

(c) $C_{\widehat{TA}}$ for Panel 5

FIG. 9. Variation in $C_{\widehat{TA}}$ during a cycle for panels 1, 3, and 5 at their respective St: (a) panel 1, $0.09 \leqslant$ St $\leqslant$ 0.41; (b) panel 3, $0.11 \leqslant$ St $\leqslant 0.53$; (c) panel 5, $0.14 \leqslant$ St $\leqslant 0.66$. The angular position of the panel is shown in gray. To-scale schematics of panel planforms shown in each subfigure.

during a pitching cycle are shown in Fig. 9. Similar to the findings for $C_{\widehat{T}}$ and $C_{\widehat{L}}$, Fig. 9 demonstrates that changes in St do not strongly influence the timings of maxima and minima in $C_{\widehat{TA}}$, despite their large impact on amplitude. However, as will be discussed subsequently, changes in planform play an important role on the timings of axial forces and their influence on thrust. The identification of key timing events in the $C_{\widehat{TA}}$ traces can be difficult because of the same high frequency oscillations observed in $C_{\widehat{T}}$. These high frequency oscillations are prominent for panels 1 and 3 in Figs. 9(a) and 9(b) at all St, and they decrease as the panel becomes more pointed while increasing with St. It is difficult to recognize at low St, but the dominant frequency at which $C_{\widehat{TA}}$ varies is twice the pitching frequency. This is similar to $C_{\widehat{T}}$, although the maxima and minima timings are different between these two quantities.

For all panels and St, peaks in $C_{\widehat{TA}}$ develop earlier in the pitching cycle than $C_{\widehat{T}}$, and they tend to occur shortly after the panel has crossed the wake centerline when $t/T \approx 0$ and $t/T \approx 0.5$. $C_{\widehat{TA}}$ minima tend to occur shortly after the panel reaches motion extremes at $t/T \approx 0.25$ and $t/T \approx 0.75$. For the more pointed panel [panel 5, Fig. 9(c)], $C_{\widehat{TA}}$ maxima and minima tend to occur earlier in the cycle closer to times when $\phi = 0°$ and $\phi = \phi_{\max}$, respectively. This shift in timing is important in demonstrating the link between increasing $C_{\overline{T}}$ and changes in axial forces. Although not shown directly in Fig. 9, the time-varying behaviors of $C_{\widehat{A}}$ closely resemble those of $C_{\widehat{TA}}$. As the trailing edge becomes more pointed, maxima in $C_{\widehat{A}}$ occur closer to angular positions of $\phi \approx 0°$, i.e., closer to times when the value of $\cos \phi$ in Eq. (1) is at a maximum and $C_{\widehat{A}}$ strongly contributes to $C_{\widehat{TA}}$ and $C_{\overline{TA}}$. Conversely, the most pointed panels experience minima in $C_{\widehat{A}}$ near portions of the

pitching cycle when $\cos\phi$ is at a minimum, i.e., negative, and small magnitude axial forces are experienced at times when they have a reduced influence on thrust production. Furthermore, the timing behaviors of $C_{\hat{A}}$ cause more pointed panels to develop high axial forces at times when their influence on lateral forces is diminished. The timings of the axial force contribution to thrust in Fig. 9 show that changes in planform shape rather than St are associated with the beneficial timing shifts in $C_{\hat{A}}$ that occur for thrust-producing panels in the current work. Accordingly, the performance enhancements associated with $C_{\hat{A}}$ behaviors should be interpreted as a property of planform and not strictly kinematics.

As evident in Fig. 9(c), the largest mean thrusts, which occur for panel 5, coincide with situations when St is high and $C_{\widehat{TA}}$ is positive throughout the pitching cycle. At low St, panels 1 and 3 experience negative $C_{\widehat{TA}}$ during extended portions of a pitching cycle, leading to below-zero values of $C_{\overline{TA}}$ that act to diminish mean thrust, even during scenarios of net thrust production. Strong secondary oscillations in $C_{\widehat{TA}}$ are a feature of panels 1 and 3 in Figs. 9(a) and 9(b), especially at high St. These high frequency axial force oscillations are responsible for for the secondary oscillations in $C_{\hat{T}}$ for panel 1 that are shown in Fig. 6(a) and were discussed in Sec. III B. These oscillations in $C_{\widehat{TA}}$ become especially strong and reduce instantaneous thrust after $C_{\hat{T}}$ reaches a maximum at times of $t/T \approx 0.35$ and $t/T \approx 0.85$. For panel 1 when St = 0.41, oscillations in $C_{\widehat{TA}}$ can results in fluctuations in $C_{\widehat{TA}}$ as large as 0.2. These rapid decreases in axial force for panel 1 occur during a part of the pitching period when thrust-producing panels, which are not subjected to such decreases in axial force, continue to increase their instantaneous thrust. Although significant $C_{\widehat{TA}}$ oscillations exist for panel 3 as shown in Fig. 9(b), their overall influence is diminished due to the contributions of normal forces.

Traces of $C_{\widehat{TN}}$ for select panels at their respective St during a pitching cycle are shown in Fig. 10. Comparison of Figs. 9 and 10 reveals that normal forces oscillate with larger amplitudes than axial forces. Similar to the findings for $C_{\hat{T}}$ and $C_{\hat{L}}$, Fig. 10 demonstrates that changes in planform and St do not strongly influence the timings of maxima and minima in $C_{\widehat{TN}}$, despite their large impact on normal force amplitude. Traces of $C_{\widehat{TN}}$ show qualitative similarities to traces of $C_{\hat{T}}$ as both reach their extremes shortly after the panel reaches a motion extreme and shortly after the panel crosses the wake centerline. This indicates that timing of phase-averaged thrust is primarily governed by normal forces, regardless of planform or St. Additionally, $C_{\widehat{TN}}$ traces are much smoother during a cycle than $C_{\widehat{TA}}$, further demonstrating that high frequency oscillations in axial forces are the cause of thrust oscillations for panel 1 in Fig. 6(a).

The presence of relatively large $C_{\widehat{TN}}$ peaks contributes to the positive values of $C_{\overline{TN}}$ for thrust-producing panels at most St in Fig. 8(b). At low St, the most forked panel (panel 1) displays larger $C_{\widehat{TN}}$ maxima than minima, but time-varying normal forces degrade rapidly after reaching a maximum, leading to $C_{\overline{TN}}$, i.e., time-averaged normal forces contributing to forward thrust, that are always negative for forked panels. As St increases past that of peak propulsive efficiency for panels 3–5, the magnitudes of $C_{\widehat{TN}}$ troughs becomes larger than $C_{\widehat{TN}}$ peaks, in agreement with the rapid decrease in $C_{\overline{TN}}$ for thrust-producing panels shown in Fig. 8(b). However, as these negative mean normal forces become more significant, their influence can be counteracted by the positive axial forces typical of thrust-producing panels. For example, $C_{\widehat{TA}}$ is positive throughout a pitching cycle for panel 5 when St = 0.66, while $C_{\widehat{TN}}$ is negative when $0 < t/T < 0.25$ and $0.5 < t/T < 0.75$, approximately. Accordingly, for some portions of the cycle when $C_{\widehat{TN}}$ is negative for panel 5 at St = 0.66, $C_{\widehat{TA}}$ is close to its maximum value and axial forces reduce the detrimental influence of normal forces. As a result, the axial forces on panel 5 either enhance the positive thrust arising from normal forces or diminish their undesirable impacts during a pitching cycle.

IV. DISCUSSION

The influence of trailing edge shape and Strouhal number on the mean and time-varying forces acting on bio-inspired pitching panels of trapezoidal planform is investigated experimentally in the range $0.09 \leqslant St \leqslant 0.66$ for a series of panels with aspect ratios of $3.0 \leqslant AR \leqslant 6.6$. Mean
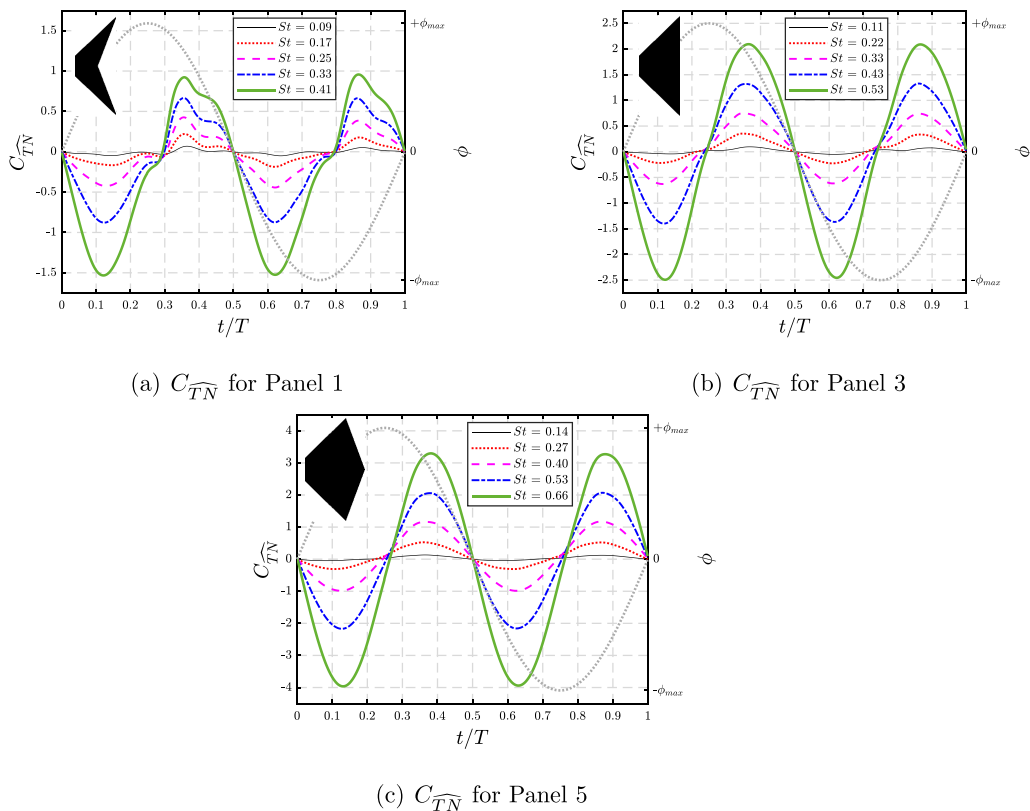
(a) $C_{\widehat{TN}}$ for Panel 1

(b) $C_{\widehat{TN}}$ for Panel 3

(c) $C_{\widehat{TN}}$ for Panel 5

FIG. 10. Variation in $C_{\widehat{TN}}$ during a cycle for panels 1, 3, and 5 at their respective St: (a) panel 1, $0.09 \leqslant$ St $\leqslant 0.41$; (b) panel 3, $0.11 \leqslant$ St $\leqslant 0.53$; (c) panel 5, $0.14 \leqslant$ St $\leqslant 0.66$. The angular position of the panel is shown in gray. To-scale schematics of panel planforms shown in each subfigure.

propulsive performance, as indicated by measurements of the coefficient of thrust and propulsive efficiency, is significantly influenced by trailing edge shape and St. In agreement with prior experimental work on rectangular pitching panels [31], trapezoidal planforms with pointed trailing edges and reduced AR produce greater mean thrust and higher propulsive efficiency. Pointed planforms outperform those with forked trailing edges and larger AR in all scenarios tested. Measurements of time-averaged thrust also demonstrate that mean performance results are more appropriately scaled using mean trailing edge velocity rather than the dynamic pressure of the free stream, in agreement with prior work that focused only on two-dimensional foils [45]. Given that AR and trailing edge sweep are varied simultaneously in the current work, it is difficult to isolate their individual influence on trends in performance. However, prior work on rectangular pitching panels have demonstrated that the mean performance of an isolated propulsor improves when the trailing edge becomes more pointed, even when AR and planform area are held constant [31,32]. With the results of these prior works in mind, it is reasonable to expect that the relatively high performance of pointed panels in the current work is due, in part, to changes in trailing edge shape, although future work and scaling laws are necessary to determine to what extent trailing edge sweep is responsible for performance. The performance results of the current work highlight the utility of three-dimensional scalings that help elucidate the form and function of biological and bio-inspired propulsors.

The results for mean propulsive performance are not anticipated given observations of animal swimmers, which indicate that caudal fins and cetacean flukes of high AR and forked or lunate planforms are characteristic of high performance swimming. It is well documented that these forked

or lunate propulsors are found in animal species that swim at high speeds during open-ocean cruising [54], and the disconnect between observations of nature and the results of the current work is worth further examination. As discussed by Tack and Gemmel [55], assumptions about the economical cruising of forked caudal fins are often made, but direct experimental comparison with truncate tails has been absent from the research literature. To remedy this absence, the energetics of truncate and forked planforms were measured experimentally. Their results show that forked tails actually require higher energetic costs during cruising than truncate planforms, even requiring some fish species to use more of their axial musculature. The authors propose that flexible forked caudal fins arose as a tradeoff between energetics and stability, and forked fins provide functionality beyond just forward propulsion as each lobe of the caudal fin can be used independently for stability and maneuvering. In light of the results of the current work and the proposals of Tack and Gemmel [55], caution should be used when generalizing specific propulsor shapes to certain functions and performance characteristics. Other factors that are relevant to swimming animals may ultimately not be captured in experiments on an isolated pitching panel of rigid material. To further understand the role of planform shape in animal propulsion, experiments and simulations on bio-inspired swimming need to incorporate biological characteristics not captured in the current work, e.g., flexibility, more complex kinematics, and an upstream body. These features have been shown to influence performance in previous simulations and experiments [38,56–58]. The propulsors of swimming animals are often incredibly complex, and they may consist of flexible fin rays, intricate musculoskeletal structures, and they may change shape and surface area during locomotion [59–61].

Results show that changes to trailing edge shape and St have significant impact on the characteristics of time-varying thrust and lateral forces. Thrust peaks shortly after the panel pitches away from a motion extreme while thrust minima occur shortly after the panel pitches across the wake centerline. The timing of force maxima and minima show relatively weak dependence on planform shape and kinematics, but some minor dependence is still present. For all panels, thrust lags the panel motion and that lag decreases during scenarios of high efficiency and increases for scenarios of large mean thrust for thrust-producing panels. Thrust timings are similar to those reported in the research literature, further indicating that significant changes to planform and pitching amplitude do little to alter the timing of forces during a pitching cycle. Lateral forces on the panel are approximately zero near when the panel changes direction at a motion extreme, and peak magnitude side forces occur when the panel pitches near the wake centerline with large angular speed. The timing of near-zero lateral forces shows almost no dependence on planform shape or St, but peak magnitude lateral forces occur later in the pitching cycle as St and trailing edge convexity increase.

Increases in St and trailing edge convexity lead to larger thrust peaks during a pitching cycle, but stronger thrust maxima are always accompanied by greater drag minima. All panels experience positive thrust during a significant portion of a pitching cycle, even when mean thrust is negative. Positive time-averaged thrust only develops when a panel experiences thrust maxima with a magnitude exceeding that of the thrust minima. Thrust amplitudes, which scale nonlinearly with St can become rather large, and are largest for pointed panels of reduced AR pitching with high mean thrust. Mean thrust for forked planforms tends to decrease with St, failing to produce positive thrust. These findings show that diverging behaviors between mean and time-varying thrust behaviors are possible, and that large thrust amplitudes are not necessarily indicative of positive mean thrust. Larger St and greater trailing edge convexity result in higher magnitude peak lateral forces, with stronger lateral forces developing for more pointed panels when St are equal or similar. Large lateral force amplitudes are associated with elevated mean thrust and high, but not necessarily optimal, propulsive efficiency. These side forces could prove useful for situations where a swimming animal or vehicle requires maneuverability. Large lateral forces, while useful for maneuvering and control surfaces, will subject the moving body to recoil reactions, which may hinder locomotion in some circumstances. Large thrust and efficiency may be accompanied by forces not generally useful for swimmers employing straight line swimming over long distances.

Force measurements in the rotating reference frame of the panel reveal how normal and axial forces contribute to mean performance. The mean behaviors of thrust-producing geometries can

be divided into two regimes, which was not observed in prior experimental work on the normal and axial forces on a pitching rigid NACA 0012 airfoil [40]. One regime is present at low St, where time-averaged normal force is the dominant source of mean thrust. The other is observed at high St, where time-averaged axial force is the dominant source. In the first regime, mean axial forces are small and tend to be negative, acting to reduce mean thrust while mean normal forces are dominant. When a thrust-producing panel pitches with relatively large propulsive efficiency at mid-range St, mean axial forces are near-zero or negative. Once a thrust-producing panel reaches a local maximum in efficiency, further increases in St result in a nonlinear increase in mean axial force, which is accompanied by a rapid decreases in mean normal force. Accordingly, the mean propulsive characteristics of the thrust-producing panels can be viewed as a tradeoff between the actions of time-varying normal and axial forces. For conditions of high efficiency, mean normal force is relatively large, while greater mean thrust occurs when mean axial force is large.

In a time-varying sense, normal and axial forces help explain the divergence in mean performance between forked and nonforked planforms. Planform has a significant impact on instantaneous axial forces. As the trailing edge becomes more pointed, peak thrust-producing axial forces become stronger and are experienced as the panel is more closely aligned with the free stream flow direction, allowing axial forces to increase their contribution to mean thrust. Conversely, more pointed panels experience their least beneficial axial forces closer to motion extremes, where the impact of axial forces are weakened due to the angular displacement of the panel. Instantaneous normal forces have significant amplitudes and they contribute strongly to the behaviors of instantaneous and mean thrust. Normal force amplitudes increase with planform and St, and they degrade thrust production to a greater degree as the trailing edge becomes more pointed or as St increases. However, the negative influences of normal forces during certain portions of a pitching cycle are reduced by the actions of axial forces for nonforked planforms. These thrust-producing panels experience positive axial forces during most, if not all, of the pitching cycle, countering undesirable effects of time-varying normal forces at larger St.

Panel forces ultimately depend on the integrated effects of surface pressure. Although pressure measurements are not available in the current work, prior research provides insight into phenomena that may occur for the panels in the current work. Unsteady pressure on a rectangular pitching panel were measured by Green *et al.* [62], who found that as the panel retreated from a motion extreme, low pressure developed on the trailing surface while positive pressure dwelt on the advancing surface. Consistent with $C_{\widehat{T}}$ behaviors in Fig. 6, the largest pressure differentials developed near motion extremes, and it is reasonable to assume that maximum instantaneous thrust developed near motion extremes due to large pressure differentials and pitch angle. Increasing AR by increasing span was shown to impede spanwise flows that relieved low pressure near the midspan, creating prolonged durations of low pressure that aid thrust production. In the current work, increases in AR are due to reductions in panel area rather than increases in span, which introduce additional surface pressure behaviors not present in rectangular panels. Despite planform differences, results in the context of rectangular panels demonstrate that beneficial pressure distributions can be promoted when flows around panel edges are inhibited. The time-varying surface pressures of AR = 1 rectangular pitching panels with varying trailing edge shape were examined by Hemmati *et al.* [32] As the trailing edge became more pointed, high and low pressure regions on opposite faces grew in size and pressure magnitude, and mean thrust and efficiency increased. Given the kinematic and geometric similarities of this previous work, it is expected that panels in the current work display similar pressure behaviors that may help explain their improved performance. The reduced thrust production of forked panels was attributed in part to the lack of pressure differential between panel faces near the spanwise tips [32]. For a forked panel, flow easily spilled over the advancing face, relieving low pressure regions critical to thrust. As a result, regions near the spanwise tips could not sustain a useful pressure differential and positive thrust resulted only from small areas near midspan rather than the larger regions observed for pointed panels. In light of the pressure results of Green *et al.* [62], the tip regions of high AR forked panels in the current work may act similarly to low AR rectangular propulsors.
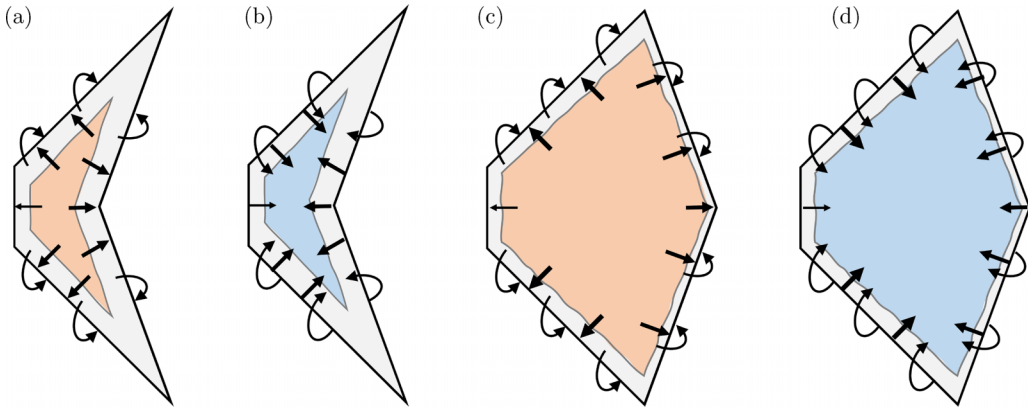
FIG. 11. Sketches of proposed surface pressure behaviors and flows on panel surfaces at times near maximum instantaneous thrust during a pitching cycle. Straight arrows represent proposed direction of flows on the panel surface that are driven by local pressure gradients, and wider arrows indicate stronger pressure gradients. Curved arrows indicate flow around the panel edges from a high pressure surface to a low pressure surface. Regions of low pressure are shown in blue, and regions of high pressure are shown in orange: (a) panel 1 high pressure surface; (b) panel 1 low pressure surface; (c) panel 5 high pressure surface; (d) panel 5 low pressure surface.

Due to the shape of the swept leading and trailing edges of the panels in the current work, it is hypothesized that the reduced surface areas, near both the midspan and spanwise tips, of the forked panels in the current work are unable to support regions of strong pressure differential that are critical for thrust production. The impact of these reduced surface areas is demonstrated using Fig. 11, which illustrates the proposed behaviors for pressure and fluid flows on the high and low pressure panel surfaces of panels 1 and 5 at times near maximum instantaneous thrust. In Fig. 11, flows along the panel surface are indicated with straight arrows, whose relative widths represent the strength of local pressure gradients driving these flows. Even though AR is relatively large for forked panels in the current work, they do not possess the ability to inhibit pressure-relieving flows that occur between high and low pressure surfaces. When panel 1 experiences large instantaneous thrust, it is at a relatively high angle of attack, with a low pressure region on the upstream face of the panel and a high pressure region on the downstream surface. Due to the spatial proximity of the 45° swept edges and the concave trailing edge of panel 1, when pressure gradients on the high pressure surface drive flows toward and around the swept and trailing edges, pressure differentials between the panel surfaces are easily relieved. This characteristic is most apparent near the spanwise tips of panel 1, where the panel edges are in close proximity, which leads to the relatively quick relief of low pressure and the inability to sustain significant pressure differentials near the spanwise tips as shown in Figs. 11(a) and 11(b). In opposition to the forked panels, low AR pointed panels like panel 5 can support stronger pressure differentials across larger surface areas due to the increased distance between swept and trailing edges, resulting in greater mean thrust. In this way, more pointed panels act similarly to the high AR rectangular panels studied by Green *et al.* [62]. The convexity of the trailing edge acts like an increase in span and inhibits the relief of low pressure surface when angle of attack is high, leading to enhanced thrust for the pointed panels in the current work. These proposed behaviors and their impact on propulsive performance still require future validation through additional experimental or numerical work.

[1] M. J. Lighthill, Hydromechanics of aquatic animal propulsion, Annu. Rev. Fluid Mech. **1**, 413 (1969).

[2] A. J. Smits, Undulatory and oscillatory swimming, J. Fluid Mech. **874**, P1 (2019).

[3] M. Barton and C. E. Bond, *Bond's Biology of Fishes* (Thomson, Stamford, CT, 2007).

[4] P. R. Bandyopadhyay, Trends in biorobotic autonomous undersea vehicles, IEEE J. Oceanic Eng. **30**, 109 (2005).

[5] P. R. Bandyopadhyay, D. N. Beal, and A. Menozzi, Biorobotic insights into how animals swim, J. Exp. Biol. **211**, 206 (2008).

[6] D. Barrett, M. Triantafyllou, D. Yue, M. Grosenbaugh, and M. Wolfgang, Drag reduction in fish-like locomotion, J. Fluid Mech. **392**, 183 (1999).

[7] T. J. Mueller and J. D. DeLaurier, Aerodynamics of small vehicles, Annu. Rev. Fluid Mech. **35**, 89 (2003).

[8] D. Roper, S. Sharma, R. Sutton, and P. Culverhouse, A review of developments towards biologically inspired propulsion systems for autonomous underwater vehicles, Proc. Inst. Mech. Eng., Part M: J. Eng. Marit. Environ. **225**, 77 (2011).

[9] R. Siddall and M. Kovac, Launching the aquamav: Bioinspired design for aerial-aquatic robotic platforms, Bioinspir. Biomim. **9**, 031001 (2014).

[10] M. S. Triantafyllou, G. S. Triantafyllou, and D. K. P. Yue, Hydrodynamics of fishlike swimming, Annu. Rev. Fluid Mech. **32**, 33 (2000).

[11] M. S. Triantafyllou, A. H. Techet, and F. S. Hover, Review of experimental work in biomimetic foils, IEEE J. Oceanic Eng. **29**, 585 (2004).

[12] J. Yu, Z. Su, Z. Wu, and M. Tan, Development of a fast-swimming dolphin robot capable of leaping, IEEE/ASME Trans. Mechatron. **21**, 2307 (2016).

[13] E. F. S. Danson, *Technology and Applications of Autonomous Underwater Vehicles* (Taylor and Francis, London, 2003), pp. 127–138.

[14] S. Corfield and C. Hillenbrand, *Technology and Applications of Underwater Autonomous Vehicles* (Taylor and Francis, London, 2003), pp. 161–178.

[15] C.-S. Lee, Y.-D. Choi, B.-K. Ahn, M.-S. Shin, and H.-G. Jang, Performance optimization of marine propellers, Int. J. Naval Architect. Ocean Eng. **2**, 211 (2010).

[16] D. Read, F. Hover, and M. Triantafyllou, Forces on oscillating foils for propulsion and maneuvering, J. Fluids Struct. **17**, 163 (2003).

[17] A. Mackowski and C. Williamson, Direct measurement of thrust and efficiency of an airfoil undergoing pure pitching, J. Fluid Mech. **765**, 524 (2015).

[18] P. Riggs, A. Bowyer, and J. Vincent, Advantages of a biomimetic stiffness profile in pitching flexible fin propulsion, J. Bionic Eng. **7**, 113 (2010).

[19] D. Floryan, T. V. Buren, C. Rowley, and A. Smits, Scaling the propulsive performance of heaving and pitching airfoils, J. Fluid Mech. **822**, 386 (2017).

[20] C. Tropea and A. L. Yarin, *Springer Handbook of Experimental Fluid Mechanics* (Springer Science & Business Media, Cham, 2007).

[21] G. Triantafyllou, M. Triantafyllou, and M. Grosenbaugh, Optimal thrust development in oscillating foils with application to fish propulsion, J. Fluids Struct. **7**, 205 (1993).

[22] G. K. Taylor, R. L. Nudds, and A. L. R. Thomas, Flying and swimming animals cruise at a Strouhal number tuned for high power efficiency, Nature (London) **425**, 707 (2003).

[23] J. H. J. Buchholz and A. J. Smits, The wake structure and thrust performance of a rigid low-aspect-ratio pitching panel, J. Fluid Mech. **603**, 331 (2008).

[24] M. Koochesfahani, Vortical patterns in the wake of an oscillating foil, AIAA J. **27**, 1200 (1989).

[25] G.-j. Li, Z. Luodin, and X.-y. Lu, Numerical studies on locomotion performance of fish-like tail fins, J. Hydrodyn. Ser. B **24**, 488 (2012).

[26] C. Li and H. Dong, Three-dimensional wake topology and propulsive performance of low-aspect-ratio pitching-rolling plates, Phys. Fluids **28**, 071901 (2016).

[27] A. Das, R. K. Shukla, and R. N. Govardhan, Existence of a sharp transition in the peak propulsive efficiency of a low-Re pitching foil, J. Fluid Mech. **800**, 307 (2016).

[28] H. Dong, R. Mittal, and F. Najjar, Wake topology and hydrodynamic performance of low-aspect-ratio flapping foils, J. Fluid Mech. **566**, 309 (2006).

[29] P. A. Dewey, B. M. Boschitsch, K. W. Moored, H. A. Stone, and A. J. Smits, Scaling laws for the thrust production of flexible pitching panels, J. Fluid Mech. **732**, 29 (2013).

[30] T. Van Buren, D. Floryan, and A. J. Smits, Scaling and performance of simultaneously heaving and pitching foils, AIAA J. **57**, 3666 (2019).

[31] T. Van Buren, D. Floryan, D. Brunner, U. Senturk, and A. J. Smits, Impact of trailing edge shape on the wake and propulsive performance of pitching panels, Phys. Rev. Fluids **2**, 014702 (2017).

[32] A. Hemmati, T. Van Buren, and A. J. Smits, Effects of trailing edge shape on vortex formation by pitching panels of small aspect ratio, Phys. Rev. Fluids **4**, 033101 (2019).

[33] C. Zhang, H. Huang, and X.-Y. Lu, Effect of trailing-edge shape on the self-propulsive performance of heaving flexible plates, J. Fluid Mech. **887**, A7 (2020).

[34] K. L. Feilich and G. V. Lauder, Passive mechanical models of fish caudal fins: Effects of shape and stiffness on self-propulsion, Bioinspir. Biomim. **10**, 036002 (2015).

[35] M. Chopra, Hydromechanics of lunate-tail swimming propulsion, J. Fluid Mech. **64**, 375 (1974).

[36] M. Chopra and T. Kambe, Hydromechanics of lunate-tail swimming propulsion. Part 2, J. Fluid Mech. **79**, 49 (1977).

[37] P. Blondeaux, F. Fornarelli, L. Guglielmini, M. S. Triantafyllou, and R. Verzicco, Numerical experiments on flapping foils mimicking fish-like locomotion, Phys. Fluids **17**, 113601 (2005).

[38] D. B. Quinn, G. V. Lauder, and A. J. Smits, Scaling the propulsive performance of heaving flexible panels, J. Fluid Mech. **738**, 250 (2014).

[39] A. Andersen, T. Bohr, T. Schnipper, and J. H. Walther, Wake structure and thrust generation of a flapping foil in two-dimensional flow, J. Fluid Mech. **812**, R4 (2017).

[40] M. J. David, R. N. Govardhan, and J. H. Arakeri, Thrust generation from pitching foils with flexible trailing edge flaps, J. Fluid Mech. **828**, 70 (2017).

[41] J. R. Nursall, The caudal fin as a hyrdofoil, Evolution **12**, 116 (1958).

[42] J. J. Magnuson, Fish Physiology, *Vol. VII: Locomotion* (Academic Press, San Diego, 1978), pp. 239–313.

[43] C. Morton and S. Yarusevych, Vortex dynamics in the turbulent wake of a single step cylinder, J. Fluids Eng. **136**, 031204 (2014).

[44] A. C. DeVoria, On the Flow Generated by Rotating Flat Plates of Low Aspect Ratio, Ph.D. thesis, State University of New York at Buffalo, 2013.

[45] T. Van Buren, D. Floryan, N. Wei, and A. J. Smits, Flow speed has little impact on propulsive characteristics of oscillating foils, Phys. Rev. Fluids **3**, 013103 (2018).

[46] F. Ayancik, Q. Zhong, D. B. Quinn, A. Brandes, H. Bart-Smith, and K. W. Moored, Scaling laws for the propulsive performance of three-dimensional pitching propulsors, J. Fluid Mech. **871**, 1117 (2019).

[47] F. Ayancik, F. E. Fish, and K. W. Moored, Three-dimensional scaling laws of cetacean propulsion characterize the hydrodynamic interplay of flukes' shape and kinematics, J. R. Soc., Interface **17**, 20190655 (2020).

[48] I. E. Garrick, Propulsion of a flapping and oscillating airfoil, NACA Report 567 (1937).

[49] M. J. Lighthill, Large-amplitude elongated-body theory of fish locomotion, Proc. R. Soc. London B **179**, 125 (1971).

[50] K. W. Moored and D. B. Quinn, Inviscid scaling laws of a self-propelled pitching airfoil, AIAA J., **57**, 3686 (2019).

[51] R. Godoy-Diana, C. Marais, J.-L. Aider, and J. E. Wesfreid, A model for the symmetry breaking of the reverse Bénard–von Kármán vortex street produced by a flapping foil, J. Fluid Mech. **622**, 23 (2009).

[52] G. C. Lewin and H. Haj-Hariri, Modelling thrust generation of a two-dimensional heaving airfoil in a viscous flow, J. Fluid Mech. **492**, 339 (2003).

[53] M. J. Lighthill, Aquatic animal propulsion of high hydromechanical efficiency, J. Fluid Mech. **44**, 265 (1970).

[54] F. F. Giammona, Form and function of the caudal fin throughout the phylogeny of fishes, Integr. Compar. Biol. **61**, 550 (2021).

[55] N. B. Tack and B. J. Gemmell, A tale of two fish tails: Does a forked tail really perform better than a truncate tail when cruising? J. Exp. Biol. **225**, 244967 (2022).

[56] E. Akoz and K. W. Moored, Unsteady propulsion by an intermittent swimming gait, J. Fluid Mech. **834**, 149 (2018).

[57] T. Van Buren, D. Floryan, D. Quinn, and A. J. Smits, Nonsinusoidal gaits for unsteady propulsion, Phys. Rev. Fluids **2**, 053101 (2017).

[58] J. Wang, D. K. Wainwright, R. E. Lindengren, G. V. Lauder, and H. Dong, Tuna locomotion: A computational hydrodynamic analysis of finlet function, J. R. Soc., Interface **17**, 20190590 (2020).

[59] R. Bainbridge, The speed of swimming of fish as related to size and to the frequency and amplitude of the tail beat, J. Exp. Biol. **35**, 109 (1958).

[60] R. Bainbridge, Caudal fin and body movement in the propulsion of some fish, J. Exp. Biol. **40**, 23 (1963).

[61] G. V. Lauder, Function of the caudal fin during locomotion in fishes: Kinematics, flow visualization, and evolutionary patterns, Amer. Zool. **40**, 101 (2000).

[62] M. A. Green and A. J. Smits, Effects of three-dimensionality on thrust production by a pitching panel, J. Fluid Mech. **211–220**, 615 (2008).